Research Square

Preprints are preliminary reports that have not undergone peer review.
They should not be considered conclusive, used to inform clinical practice,
or referenced by the media as validated information.

TiO_2–Hydroxyapatite Nanocomposite: A High-Performance Sensing Material for Volatile Organic Compound Detection

Ravi Kumar Pandey
University of Lucknow
R. R. Awasthi
Khwaja Moinuddin Chishti Language University, Lucknow, U.P.
R. K. Shukla
shuklark464@gmail.com

University of Lucknow

Research Article

Keywords: Hydroxyapatite (HaP), Titanium dioxide (TiO_2), Nanocomposite, Solid-state processing approach, Biocompatible

Posted Date: November 18th, 2026

DOI: https://doi.org/10.21203/rs.3.rs-11241501/v1

License: This work is licensed under a Creative Commons Attribution 4.0 International License.
Read Full License

Additional Declarations: No competing interests reported.

TiO_2–Hydroxyapatite Nanocomposite: A High-Performance Sensing Material for Volatile Organic Compound Detection

Ravi Kumar Pandey[1], R. R. Awasthi[2], and R. K. Shukla[1]

[1] Department of Physics, University of Lucknow, Lucknow-226007 U.P. India

[2] Department of Applied Science and Humanities (Physics), Khwaja Moinuddin Chishti Language University Lucknow-226013 U.P. India

shuklark464@gmail.com

Abstract

In this study, the synthesis, characterisation and VOC sensing behavior of TiO_2–Hydroxyapatite (HaP) nanocomposites have been systematically explored. Using chemical co-precipitation technique, HaP was obtained in a simple and economical manner. To achieve enhanced crystallinity and stability, the sample was subjected to sintering at 800 °C for 6 hours in a muffle furnace with a controlled heating rate of 5 °C/min. Subsequently, the TiO_2 nanomaterial was integrated into the HaP matrix at incremental proportions (0.5, 1.0, 1.5, and 2.0 wt%) via the solid-state processing approach. Detailed evaluation of pure and composites samples covering structural, morphological, and chemical aspect were subjected to (XRD), X-ray diffraction, (FESEM), Field emission Scanning electron microscope, (EDX), Energy-dispersive X-ray spectroscopy, Raman spectroscopy, and (XPS) X-ray photoelectron spectroscopy. The incorporation of TiO_2 modified the phase and surface features of HaP composites. These composite samples were subjected to analyse for (VOCs) volatile organic compounds (ethanol, methanol, propanol, and acetone) sensing in ambient atmosphere. Notably, among all the composite samples, composite one wt% TiO_2 loaded had strongest performance against acetone vapors due to better surface reactivity and charge transport behaviour of TiO_2 and HaP. As the result 1.0 wt% TiO_2–HaP composite is a cost-effective, biocompatible material with strong potential for real-time acetone sensing.

Keyword: Hydroxyapatite (HaP), Titanium dioxide (TiO_2), Nanocomposite, Solid-state processing approach, Biocompatible.

Corresponding Author: Ravi Pandey

Email: pandeyravik15@gmail.com

1. Introduction:

The abundance of hazardous gases, in the environment put the severe concern regarding ecological damage, humans and other living being health due to expansion of industries. But on the other hand the industrialization is also necessary to develop the nation and to ease the human life. Therefore, we need a mechanism which can detect the cause of environmental damage and alert us to act timely to overcome. A counterbalance must be established between the processes of industrialisation, which causes the environmental damage alongside the implementation of effective strategies for damage control. Now a days naturally occurring, mineral-derived compounds particularly hydroxyapatite (HaP, $Ca_{10}(PO_4)_6$ $(OH)_2$), have emerged as promising candidates for use in sensing applications. Their inherent surface architecture provides required chemical activity thereby reducing the need of complex processing steps. The hydroxyapatite (HaP, $Ca_{10}(PO_4)_6$ $(OH)_2$), valued for its biocompatibility and eco-friendly nature stands out as a strong material in sensor applications. [1–4]. Also it is recognized as a versatile material for environmental remediation such as pollutant removal and analytical monitoring [5]. This material has shown its application in water purification, particularly in removal of heavy metals from contaminated water. It has been reported that up to 80% of dissolved nickel could be adsorbed, while copper removal exceeded 87%, due to intrinsic porosity of HaP, which enables it to act as a natural adsorbent under near-neutral pH conditions [6]. Furthermore, adjusting synthesis, sintering, pH, and dopants, HaP's structure can be reshaped to enhance heavy metal uptake and reduce environmental pollution [7]. Beyond metal ion adsorption, biocompatible HaP has also been validated as an effective adsorbent for both anionic and cationic dyes, compounds whose complex molecular geometries typically resist conventional wastewater treatment. Further, introduction of oxide dopants, even in trace amounts, has been shown to further augment HaP's dye-capture efficiency [8]. Beyond dyes and metals nanoscale HaPs can also purify wastewater by removing radioactive and organic pollutants. [9]. In contrast, nano size HaP combined with the biopolymers (gelatin, chitosan, or chitin) exhibits enhanced retention capacity [10,11]. Further investigations on Sn-modified calcium phosphate have show selective Cr (Chromium) retention**,** controlled by the Sn^{2+} oxidation state during reduction-based water treatment [12, 13]. However, TiO_2–hydroxyapatite nanocomposites exhibits good photocatalytic activity under ultra violet (UV) irradiation as a result it degrade pharmaceutical contaminants such as ciprofloxacin and ofloxacin [14]. Ag-TiO_2–hydroxyapatite composites shown to have better photo-catalytic activity

for air born acetone under the exposure of visible light [15] . HaP with metal and metal oxide has also shown to have gas-sensing properties [16]. Now days metal oxide sensors are used over gas sensors for environmental surveillance as well as biomedical diagnostics [17], as their ruggedness, sensitivity, and cost effective fabrication. For example, TiO_2 nanoparticles detect SO_2 at levels as low as 50 ppm under UV light, within 298–473 K [18]. Further thin films of nanocrystalline TiO_2 exhibited strong selectivity for (H_2S) Hydrogen sulfide, responses reaching of 112,000% at 50 ppm and 85% at 100 ppb [19]. Whereas, SnO_2 nanoparticles with uniform morphology sensed NO_2 effectively, showing the responce value 35.83 at 100 ppm and maintaining repeatability and durability [20]. In comparision to HaP, HaP–graphene oxide nanocomposite containing 2 wt% grapheme oxide (GO) shows good sensitivity of detection for low ammonia level down to 10 ppm [21].

Further since unmodified HaP, shown to have poor electronic conductivity and slow response kinetics, significantly constrain its effectiveness as standalone sensing material [22]. In order to enhance these properties, HaP was combined with oxides of Ti, Zn, and Sn, which significantly improved both the Pollutant degradation and gas-monitoring capability of the composite.

within these oxides of metal, Titanium oxide is valued for stability, mobility, non-toxicity, and photocatalytic strength, making it common in photocatalysis [23], photovoltaics [24,25], and gas sensing applications [26,27]. Since HaP paired with Titanium dioxide enhances electronic and sensing properties of HaP and it could possibly be used to detect analytes. Since volatile organic compounds (VOCs) constitute a particularly relevant class of analytes, they serve as a key motivation for this study. Further since the airborn VOCs, under the exposure of sunlight undergo photochemical reactions with nitrogen oxides produces ozone and reduced air quality [28]. Exposure of VOCs may cause short-term issues like nausea and reduced focus, and long-term risks including liver damage, Central nervous system suppression, and cancer [29]. A common ketone (acetone) and industrial alcohols such as C_2H_5OH, CH_3OH, and C_3H_7OH, are frequently crossing safe limits without clear signs. This issue demands a biocompatible sensors that detect hazardous environments at room temperature. In this study we prepared TiO_2-dispersed HaP nanocomposites via solid-state synthesis approch. Nanocomposites crystallinity and physic-chemical properties were investigated by (PXRD) Powder x-ray diffraction, (FESEM) Field emission scanning electron microscopy, (EDX) Energy-dispersive X-ray spectroscopy, Raman Spectroscopy and (XPS) X-ray photoelectron

spectroscopy. The study is structured into four parts: section 2 provides the details of the experimental description, Section 3 presents results with discussion, and Section 4 concludes the work.

2. Experimental

2.1 Materials Used: All reagents of analytical grade were employed directly without further purification. Calcium nitrate tetrahydrate $Ca(NO_3)_2.4H_2O$, Ammonium dihydrogen phosphate $[(NH_4)H_2PO_4]$ served as the calcium and phosphate precursors, respectively while ammonia solution (NH_4OH) was employed to adjust the pH of the reaction medium. Titanium dioxide (TiO_2) was used to preparation of composite

2.2 Preparation method: Pure hydroxyapatite (HAP) was produced by chemical co-precipitation technique mentioned in literature [30]. 0.1 M (Molar concentration) $Ca(NO_3)_2.4H_2O$ solution was prepared using deionized (DI) water in a volumetric glassware (250 ml) and mixed using a magnetic stirrer for 15 minutes, to obtain the homogeneous solution and dissolved with calcium nitrate tetra-hydrate solution. Then, 0.06 M $(NH_4)H_2PO_4$ solution was gradually introduce drop wise under uniform stirring while control the pH 10 using ammonium hydra-oxide solution (NH_4OH). The colloidal suspension was stirred for 24 h, to promote complete reaction between calcium and phosphate ions and to allow uniform nucleation of sample. The suspension was centrifuged at 4500 rpm for 15 min and collect the white precipitate, washed repeatedly with deionized water and dried at 100 °C temperature for 12 hrs. The dried powder underwent sintering at 800 °C for 8 hours in a muffle furnace at a fixed heating rate of 5 °C/min. to enhance crystallinity, remove residual organics and stabilize the HaP phase. The net chemical reaction proceeds as:

$$10\,Ca(NO_3)2{\cdot}4H_2O + 6(NH_4)H_2PO_4 + 14NH_4OH \rightarrow Ca_{10}(PO_4)6(OH)_2 + 20NH_4NO_3 + 52H_2O$$

Various composites of pure HaP and TiO_2 in a system $xTiO_2$–(100–x) HaP were prepared by Solid-state processing approach, where x represents 0.5, 1.0, 1.5, and 2.0 wt%. Hydroxyapatite and TiO_2 were combined in stoichiometric ratios mention in above compositions were mixed and grind in acetone media using mortar and pestle. Acetone was added during mixing to improve dispersion and simultaneously minimize agglomeration of the powder particles. The prepared samples were then heated at 600 °C for 5 hrs with heating rate of 5 °C/min. in muffle furnace, to enhance the crystallinity of composite samples. The flow chart of synthesis of HaP and TiO_2 dispersed HaP is shown in fig. (1) (a) & (b) respectively.

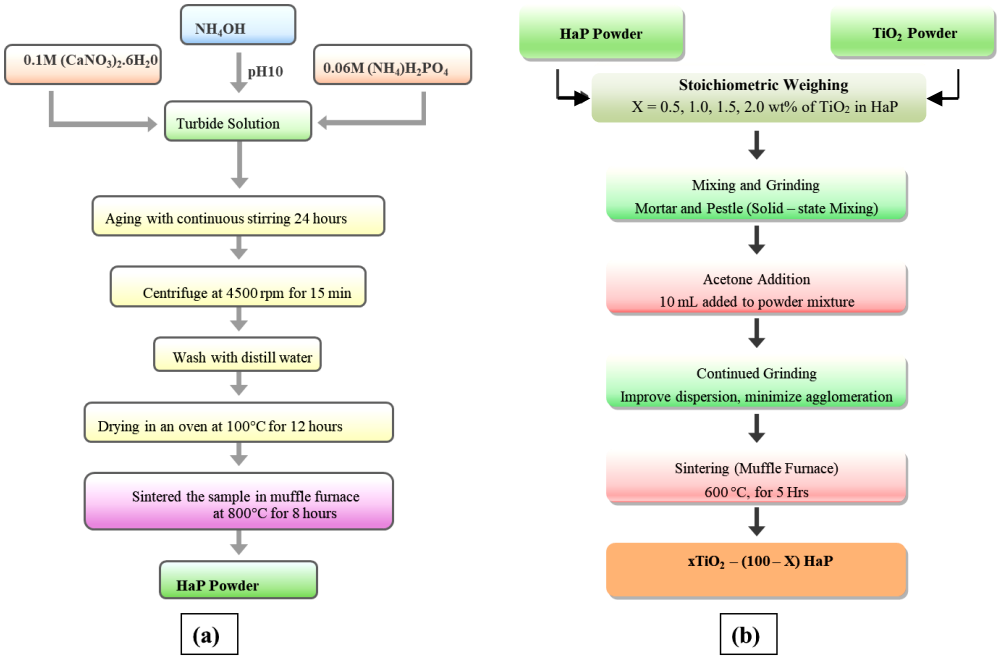


Fig.1 (a) Flow chart for synthesis of Hydroxyapetite (b) TiO_2 dispersed Hydroxyapetite nanocomposites.

2.3 Measurement of crystallinity: The crystal structure, phase stability, and purity of synthesise HaP sample along with the influence of TiO_2 incorporation into the HaP matrix, were investigated using Powder X-ray Diffraction (PXRD). The measurements were executed by a Rigaku Ultima IV operated using CuK_α source (wavelength (λ) = 1.5403 Å**).** The diffraction profiles exhibited distinct and sharp peaks, confirming the high crystallinity of the synthesized powder sample (Fig. 2). The diffraction profile of synthesize powder sample was confirmed with the data provided in (JCPDS) Joint Committee on Powder Diffraction Standards matches well with card no. 09–432. Further the crystallite dimensions of all powder samples were estimated through the Debye–Scherrer relation [31].

$$D = K\lambda / (\beta \cos\theta) \quad \text{---------- (1)}$$

Where D denote the crystalline size of the sample, K is shape factor (taken as 0.89 for spherical shape), λ is wave length of X-Rays CuKα (λ = 1.5406 Å), **β** denotes FWHM (full width at half maximum) in radians, and **θ** represents Bragg diffraction angle in radians.

2.4 Field Emission Scanning Electron Microscopy (SEM): FESEM (Carl Zeiss, Model GEMINI 560) was employed to investigate the morphology of pure HaP, TiO_2, and TiO_2 incorporated HaP nanocomposites. All images were recorded at the same resolution 50KX.

2.5 Energy Dispersive X-Ray Analysis (EDXA): In order know the stoichiometric concentration, of various elements abundance in the sample, we performed the energy dispersive X-Ray analysis (EDXA). The EDX used in this measurement was made from Carl Zeiss, Model GEMINI 560 give the knowledge of weight percentage of the elemental abundance in the sample prepared, provide a controllable switch for stoichiometric concentration for a desired sample preparation.

2.6 Raman Spectroscopy: In order to know the vibrational modes of structural units and structural integrity of HaP, TiO_2 and TiO_2 dispersed Hydroxyapatite. The Raman spectra of the samples have been performed using Raman spectrograph made from WI Tech alpha 300 RAs spectro photometer with a 532nm laser source and 600 lines per mm grating were used to analyse the samples. Raman peaks helps us to identify the vibrational modes of chemical bonding, symmetric and antisymmetric stretching vibrations. This approach provides direct insight into the bonding environment and underlying structural mechanism of the synthesied samples. For this study Raman spectrum were recorded across the wavenumber interval of 100–4000 cm^{-1}.

3. **X-ray Photoelectron Spectroscopy (XPS):** XPS analysis was conducted on a Physical Electronics (PHI) 5000 Versa Probe III using Al Kα radiation source (energy ≈1486.6 eV) under (UHV) ultra high vacuum conditions. Wide-range Survey data were obtained at 280.0 eV pass energy to identify the surface elemental composition. For a more precise evaluation of oxidation states and bonding environments, high resolution core-level spectra were obtained at pass energy of 55.0 eV. The recorded spectra were subsequently analyzed to elucidate the surface chemical composition and bonding environments present in the sample.

4. **Results and Discussion:**

In order to examine the effect of TiO_2 mixing in the hydroxyapatite (HaP) matrix, the prepared sample of varying stoichiometry (see Fig. 2) were examined using Powder X-ray diffraction (PXRD) technique. For comparative study, PXRD measurements were also performed on pure TiO_2 and pure HaP samples. The corresponding diffraction peaks for all samples are presented in Fig. 2. The XRD profile of the powder sample was validated against the (JCPDS) Joint Committee on Powder Diffraction Standards database and showed a good match with card no. 09-432. The diffraction reflections observed at (002), (102), (210), (211), (300), (202), (310), (222), (313),

(213), (321), (410), (402), and (004) planes confirm the successful formation of hydroxyapatite (HaP). Further, the reflection corresponding to Pure TiO_2 at (101), (004), (200), (105), and (211) planes are characteristic of TiO_2 in its anatase phase. [32,33]. Whereas XRD patterns of TiO_2-HaP nanocomposites shown to maintain crystalline structure at various stoichiometric concentrations (refer Fig. 2). The observed HaP peaks in the nanocomposites are more dominant, in comparison to TiO_2 peaks as smaller Wt% of TiO_2 (0.5–2.0 wt%) in HaP matrix. The crystalline size of all synthesized powder samples werw estimated using the well known relation Debye–Scherrer $D=K\lambda /(\beta \cos\theta)$, Where D denotes the avarage crystallite size, K is shape factor (0.89 taken for spherical particles), λ is X-rays wavelength (CuKα = 1.5406 Å), **β** denotes the full width at half maximum (FWHM) of the diffraction peaks in radians. The parameter 2θ corresponding to Bragg angle of the respective reflection. . The average crystallite size were evaluated and verified as 30.47, 65.55, 28.75, 32.30, 47.29 and 31.31 nm, of synthesized powder sample Hydroxyapetite, TiO_2, and (0.5- 2.0 Wt%) TiO_2 integrated HaP respectively.

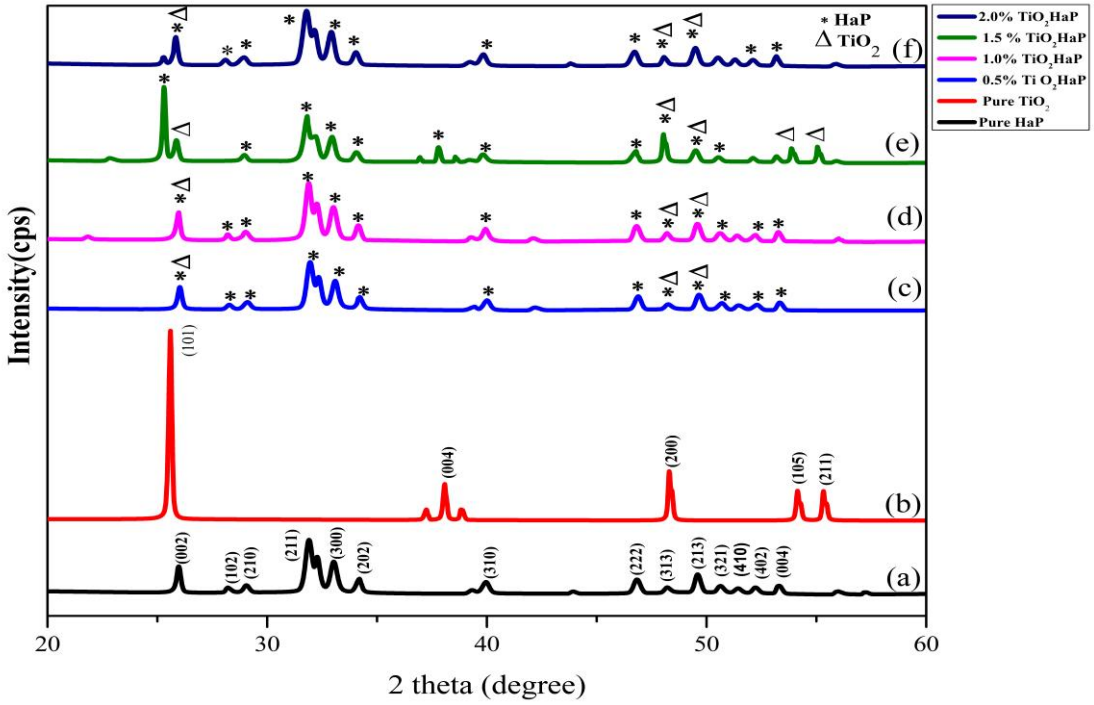


Fig.(2) XRD of (a) Pure HaP,(b) Pure TiO_2 (c-f) 0.5Wt%-2.0 Wt% TiO_2 dispersed

Further to analyse the elemental abundance and their weight percentage in various samples prepared, energy dispersive X-Ray (EDX) has been performed for each samples under study. The EDX spectrum is shown in fig.3

(a)-(f). Fig 3 (a) shows pure HaP spectrum and confirms abundance of Calcium (Ca), Phosphorous (P), and Oxygen (O) and presence of the Ti and O element in TiO_2 is shown in Fig 3 (b). Fig. 3(c)–(f) display the EDX spectra of HaP -TiO_2 nanocomposite containing 0.5-2.0 wt% TiO_2. These spectra clearly reveal the presence of calcium (Ca), phosphorus (P), oxygen (O), and titanium (Ti) in all prepared composite samples. The quantitative elemental compositions have been systematically summarized and presented in table.

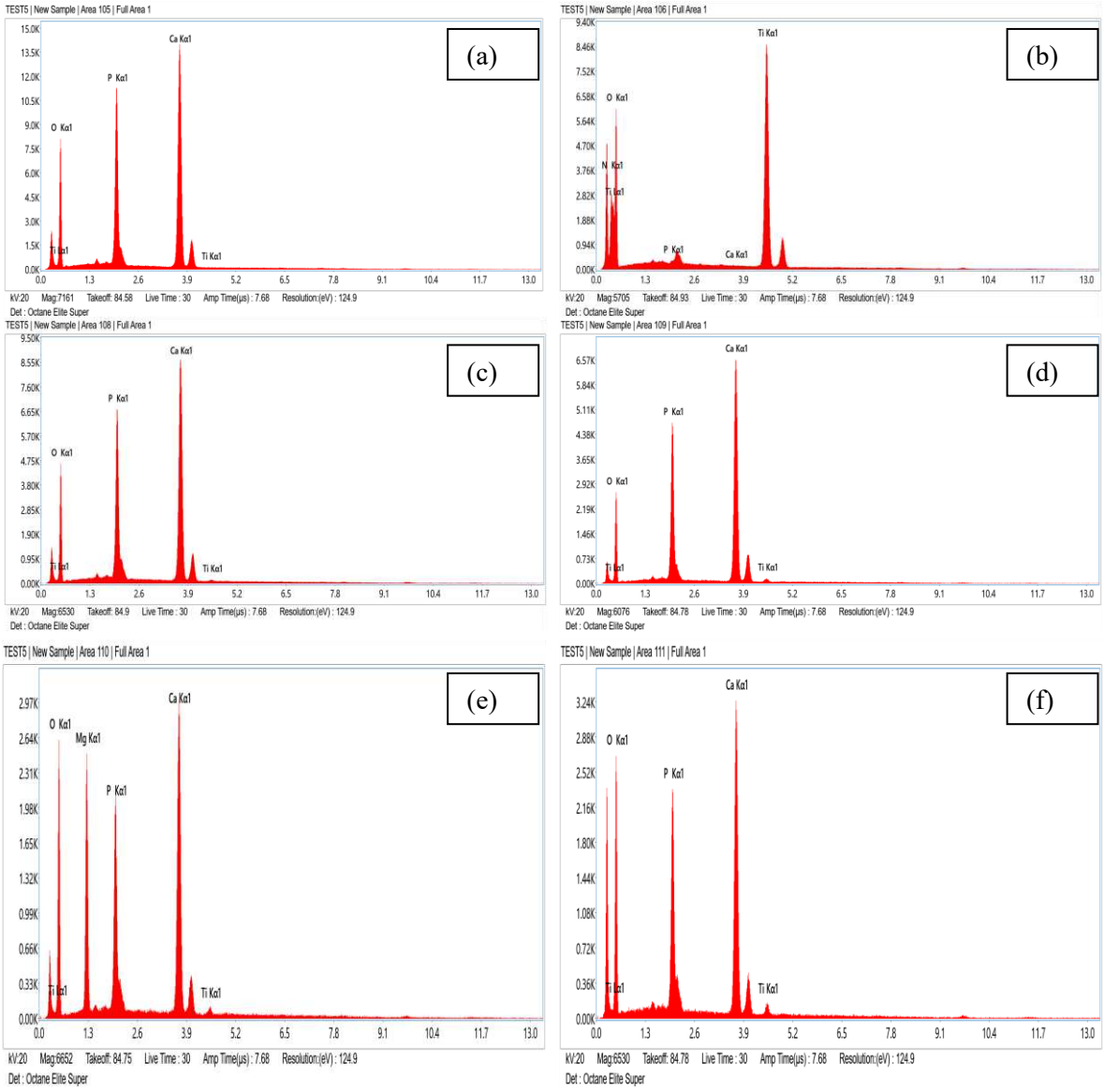


Fig. (3) EDX profile of (a) Pure HaP (b) TiO_2 (c-f) 0.5 wt% -2.0 wt% TiO_2 dispersed HaP nanocomposites.

Elements	**Pure HaP**	**TiO_2**	**0.5Wt% TiO_2 HaP**	**1.0Wt% TiO_2 HaP**	**1.5Wt% TiO_2 HaP**	**2.0Wt% TiO_2 HaP**
O (Oxygen)	**34.8**	**39.4**	**32.6**	**28.6**	**36.7**	**41.6**
P (Phosphorus)	**17.5**	**0.5**	**17.3**	**17.2**	**12.6**	**14.2**
Ca (Calcium)	**47.6**	**0.1**	**49.8**	**53.1**	**38.8**	**42.3**
Ti (Titanium)	**0.1**	**57.5**	**0.4**	**1.1**	**1.0**	**1.9**

Fig. 3 (c) shows that 0.5 wt% TiO_2 dispersed HaP sample, Ca and P peaks remain stronger as in pure sample and smaller Ti peak, shows initial incorporation of TiO_2 nanoparticles. As the concentration of TiO_2 enhanced to 1.0 wt% TiO_2–HaP, the observed enhancement in Ti peak indicating partial surface coverage by TiO_2. However, 1.5 wt% TiO_2 dispersed HaP, Ti signal becomes more pronounced, Ca and P peaks comparatively lower due to dilution effect. Further 2.0 wt% TiO_2–HaP sample shown to have Ti peak domination alongside O, whereas Ca and P signals further suppressed, confirming maximum TiO_2 dispersion in the HaP matrix.

The morphology of prepared powder samples were investigated using field emission scanning electron microscope (FESEM) and the related micrographs are presented in Fig.4. Each images were obtained at magnification of 50KX. Fig. 4 (a) shows FESEM image of pure HaP revealing a Agglomerated particles forming a disordered and porous framework. Fig. 4 (b) depicts the morphology of TiO2 nanoparticles, exhibiting nearly spherical particles with a cauliflower–like texture. However Fig. 4 (c)-(f) display FESEM micrographs HaP nanocomposites containing 0.5-2.0Wt% TiO_2. The fig 4 (c-d) represent the 0.5 and 1.0 wt% TiO_2 integrated HaP composite shows agglomerated and irregular particle distribution throughout the sample. With elevated TiO_2 content from 1.0 to 1.5 wt% in HaP matrix, a uniform distribution of the particles is appear while maintaining the porous structure of the sample, reflecting improved interfacial contact of grains. However, at the 2.0 wt% dispersion of TiO_2 in HaP indicate the dense clustering and covering most of the HaP surfaces and reducing porosity.

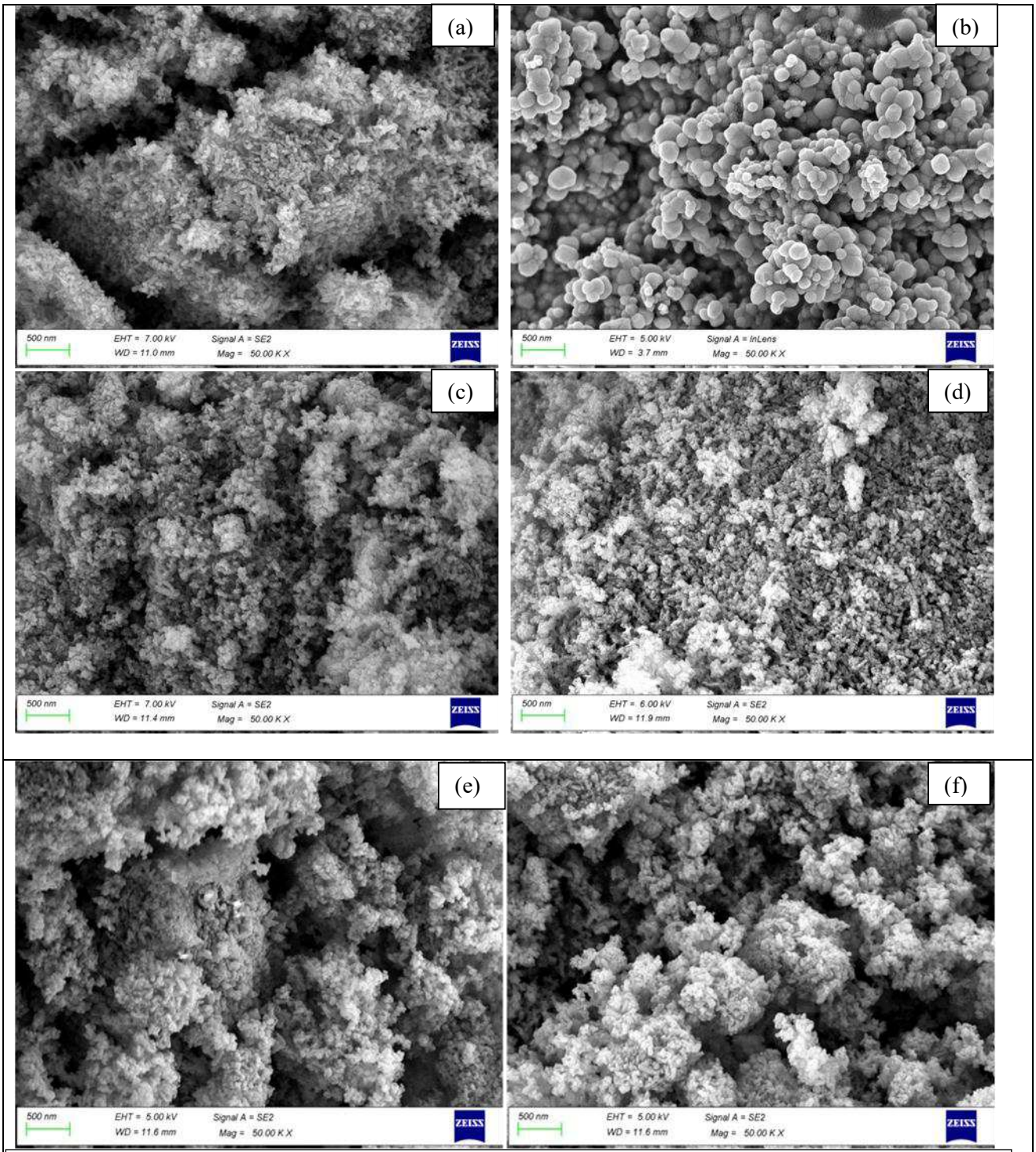


Fig. 4. FESEM image of (a) Pure HaP (b) TiO_2 (c-f) 0.5wt% -2.0 wt% TiO_2 dispersed HaP

Further the Raman spectral data of the pure HaP, TiO_2 and TiO_2 incorporated HaP, nano-composites are displayed in Fig.(5). For HaP, prominent band at 962 cm^{-1} originating from symmetric stretching of the PO_4^{3-} groups [34]. Peaks at the 433 cm^{-1} associated with symmetric stretching vibration of the phosphate ions while the peak observed around 590 cm^{-1} arises from anti-symmetric bending vibrations of the PO_4^{3-}group [35,36]. A broad feature near 3569 cm^{-1} indicates the O–H stretching mode, confirme the (OH^-)groups in the HaP lattice[37]. The weak intensity of the O–H stretching band implies negligible distortion in the HaP lattice. In case of TiO_2 Raman peaks observed at 144, 396, 517, 630 cm^{-1} are characteristic of the antase phase. Specifically, the bands at 144 & 639 cm^{-1} corresponding to Ti-O stretching, the peak at 517 cm^{-1} (A1g + B1g) refer to Ti-O stretching and at 396 cm^{-1}, the Eg band is linked to O–Ti–O bending vibrations [38,39].

For the TiO_2-dispersed HaP composite (0.5 wt% to 2.0 wt%) the Raman spectra exhibit vibrational modes of both HaP and TiO_2 , that validate effective dispersion of TiO_2 within the HaP matrix. Fig 5 shows that as the concentration of TiO_2 in HaP matrix, getting enhanced, the observed Raman peak intensity related to TiO_2 also enhanced whereas the characteristic Raman peak intensity corresponding to pure HaP remains unchanged. Further, the TiO_2-related Raman spectra in 1.5 wt% TiO_2-dispersed HaP, is found to be broadened. This broadening is due to TiO_2–HaP interfacial interactions; lattice distortion induced by heterogeneous incorporations in the pure HaP matrix, and phonon confinement effects attributed to the nanoscale dimensions of the composites. Also, at 2.0 wt% TiO_2 dispersed HaP the Raman signal of TiO_2 becomes intense, showing its higher presence in the HaP matrix. The intense broad peak points to lattice distortion and particle clustering at this loading of TiO_2 in HaP.

It is observed from fig 5 that at lower loading of TiO_2 (0.5 wt%, 1 wt%), in HaP matrix, pure HaP Raman spectra confirms the structural stability of the host matrix. Further, increasing the loading of TiO_2 (1.5 wt%, 2.0 wt%) in HaP matrix, the intensity of the HaP-related Raman peaks decreases. This reduction arises from partial coverage of HaP grains by TiO_2, which effectively marks the Raman-active PO_4^{3-} groups. As a result, the Raman signals from HaP become weaker, leading to diminished peak intensity while the peak positions remain unaffected.

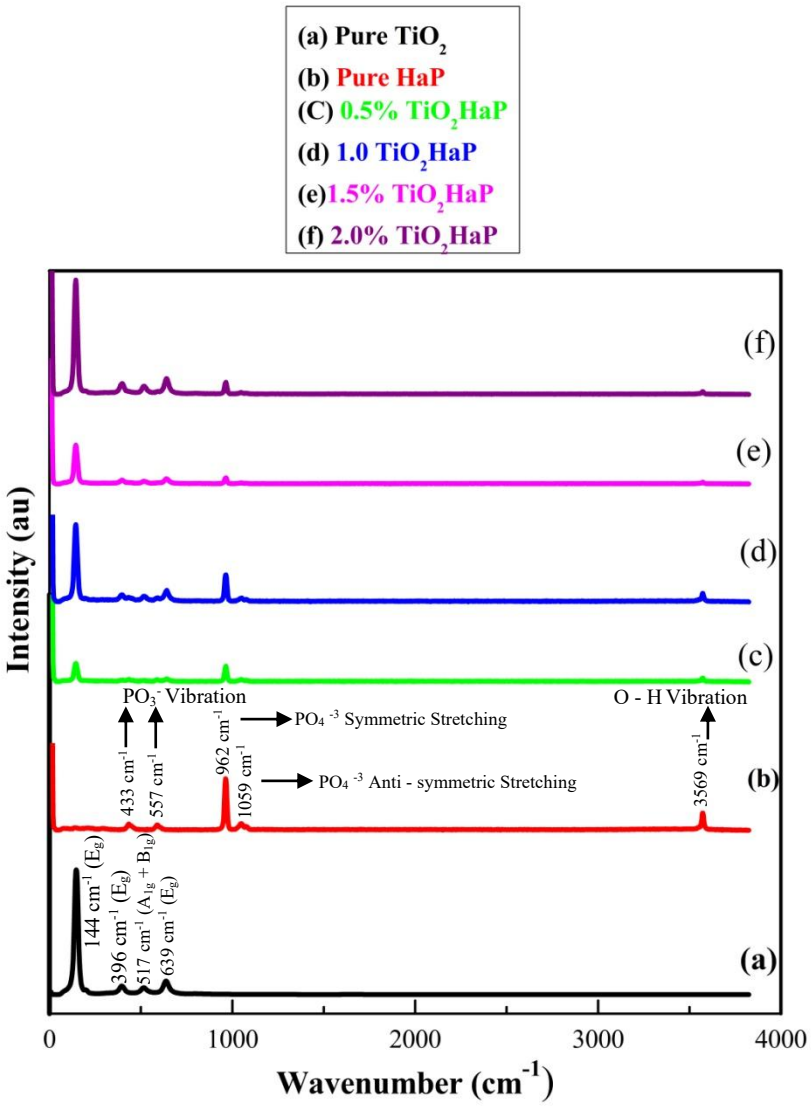


Fig. 5. Raman spectra of (a) TiO_2 (b) Pure HaP (c-f) 0.5 wt% -2.0 wt% TiO_2 dispersed HaP.

In order to know the elemental composition and chemical bonding present in the prepared powder samples XPS was executed. Fig 6.a shows the survey spectrum of HaP having distinct peaks corresponding to Ca 2p (345 eV), 2s (438eV) , P 2p (131eV), 2s (188 eV) and O 1s (529 eV). These signals confirm the presence of calcium , phosphorus and oxygen are building elements, aligns with the stoichiometric formula $Ca_{10}(Po_4)_6(OH)_2$ of hydroxyapetite [40].

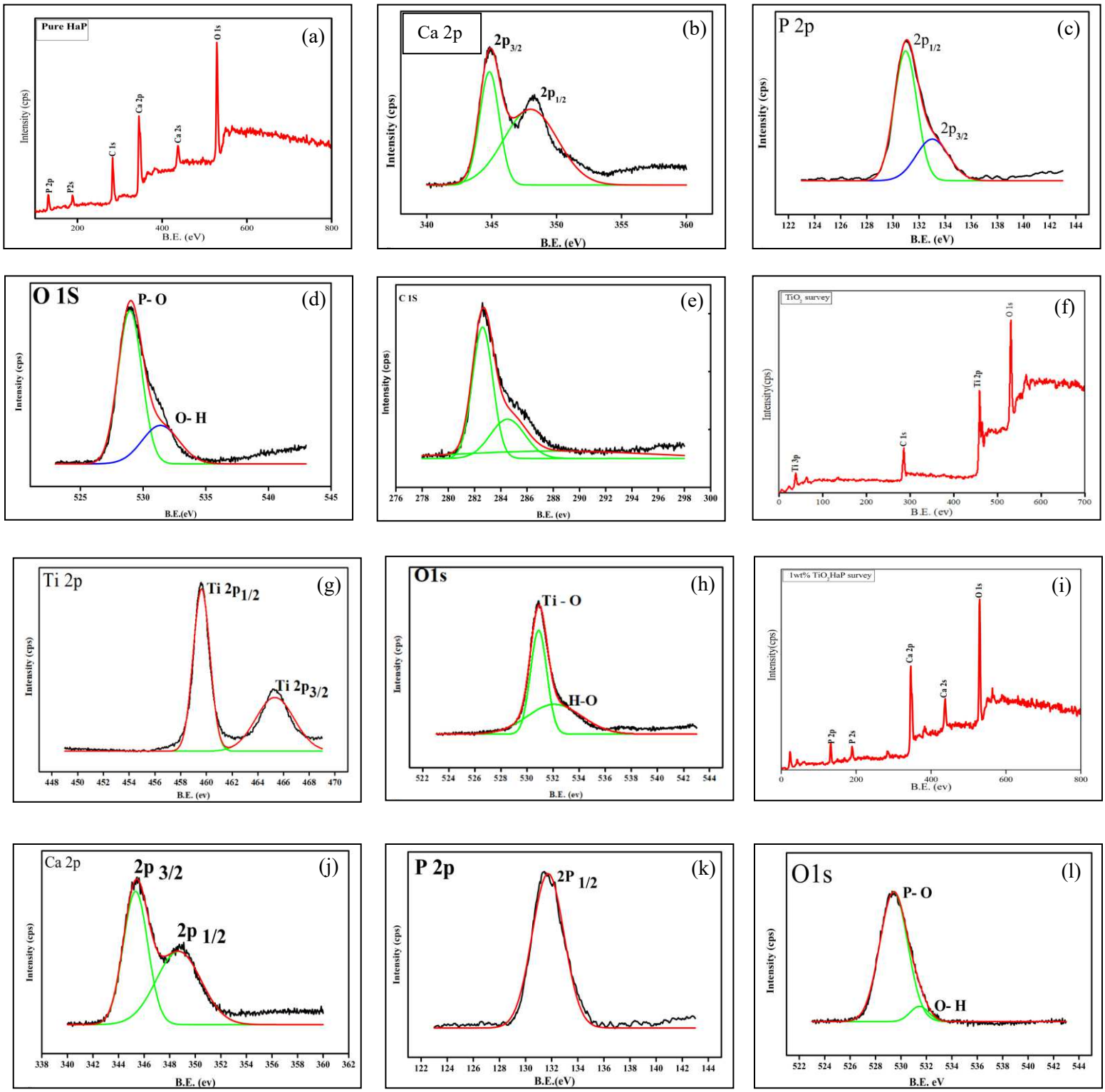


Fig. **(a).** XPS survey spectrum of HaP **(b).** Ca 2p spectrum **(c).** P 2p spectrum **(d).** O 1s spectrum **(e).** C 1s spectrum **(f).** survey spectrum of TiO_2 **(g).** Ti 2p spectrum **(h).** O 1s spectrum **(i).** survey spectrum of 1 wt% TiO_2 Dispersed HaP **(j).** Ca 2P spectrum **(k).** P 2p spectrum **(l).** O 1s spectrum.

Surface carbon contamination was attributed by minor carbon C 1s signal indicate at 285eV. Figure 6(b) the high-resolution Ca 2p spectrum, reveals two spin orbital spliting at Ca $2p_{3/2}$ (346.5 eV) and $2p_{1/2}$ (350.1 eV), with in energy gap 3.6 eV, indicating Ca^{2+} ionic sates within the apetite lattice.

Similarly the P2p spectrum shows two components at P $2p_{3/2}$ (~132.0 eV) and $2p_{1/2}$ (~133.2 eV), characteristic of (PO_4^{3-}) groups. Fig.6 (d) The spectrum of O1s exhibits pair contributions one at (531 eV) to corresponding to P–O bonds and another at (532.5 eV) associated with O–H group, confirming the coexistence of phosphate (PO_4^{3-}) and hydroxyl group within the HaP framework [41-42]. Fig. 6 (e) survey spectrum of TiO_2 clearly reveal that presence of titanium, oxygen and along with a minor trace of carbon, no additional peaks were finded, that indicating the phase purity of the sample. The Ti 2p peak appeared near 460 eV, while a strong O 1s signal was detected at 530 eV. A Ti 3p feature was also observed at the lower binding energy region at 37 eV [43]. Closer inspection of oxygen spectrum revealed slightly asymmetry in peak shape, suggesting oxygen exists in more than single chemical bonding environment.

A binding energy at 530.9 eV corresponding to strong interaction of oxygen with titanium atoms in the bulk region leading to formation of the typical Ti–O–Ti framework of TiO_2 structure. Another peak at 532.1 eV, indicate the presence of surface hydroxyl groups, likely due to adsorption of moisture from the surrounding atmosphere. The titanium region further displayed two distinct spin–orbit components, with Ti $2p_{1/2}$ and Ti $2p_{3/2}$ peaks confirming the characteristic electronic states of Ti^{4+} in the oxide lattice [44].

Fig 6 (i) shows the survey spectrum of nanocomposite 1wt% loading of TiO_2 in HaP indicate the distinct peaks corresponding to Oxygen 1s, Calcium 2p and 2s, Phosphorous 2p, and 2s, which are characteristic of HaP. These observations confirm that the surface composition is primarily dominated by HaP, as expected since TiO_2 was incorporated in a small fraction (~1 wt%). The absence of detectable Ti peaks in this spectrum is attributed to its very low concentration, which not measurable within the sensitivity range of the instrument.

The Calcium 2p spectrum with high-resolution shows two distict peaks at 346.5 eV and 350.1 eV, with energy difference 3.5eV, confirming the presence of Ca^{2+} ionic states within the hydroxyapatite lattice. The O 1s spectrum, after deconvolution, reveals two contributions a dominant peak at 530 eV attributed to P–O bonds of PO_4^{3-}, and a smaller shoulder at 531.9 eV corresponding to O–H groups that are integral part of HaP matrix.

The coexistence of these peaks validates the hydroxyl-containing phosphate framework in composite. However in pure HaP the peak position of the P–O appears at 529 eV whereas in the composite it shifts to ~530 eV. The 1 eV shift suggested that some oxygen atoms involved with bonding of Ti–O–P between TiO_2 and HaP interface. Since oxygen of TiO_2 matrix also lies in the similar energy range of 529.5 to 530.5 eV, the observed shift indicates chemical interaction between the two phases. Such interfacial bonding enhances the structural stability of nanocomposites. The P 2p spectrum further displays a broad peaks around 132-1333 , consistent with phosphate groups in the composite matrix.

Gas Sensing Applications:

We utilized a hydraulic press machine to make pallets of the aforementioned samples of different stoichiometries with standard set dimensions of 10 mm in diameter and 5 mm in thickness in order to test gas sensing applications. Electrical contacts were put evenly to the pallet's surface using silver paste. The prepared pallet was placed within a specially constructed 250 cubic centimetre (cc) airtight cubical chamber that was outfitted with a hot plate, thermocouple, High-accuracy digital millimetre instrument, fan and vacuum pump. Figure 7(e) depicts the gas measurement setup at ambient temperature. To reach the required vapor concentration, a determined amount of every (VOC) volatile organic compound such as C_2H_5OH, CH_3OH, and C_3H_7OH and acetone was injected using a syringe into a prepared sealed chamber. In air and the presence of VOC the resistance of the pallet was then recorded in order to gage response. At room temperature (28˚C), the sensing capability of the produced TiO2 dispersed HaP nanocomposite was tested. The expression is used to quantify the sensor's response (R) [45].

$$R = \frac{R_a - R_g}{R_a} x100$$

Where Rg indicate the resistance measured after the pallet based sensor acheived a stable value in the presence of VOC vapor, and Ra is the pallet's baseline resistance measured in the presence of air. Response and recovery times were measured in order to assess the pallet-based sensor's sensing capabilities. Recovery time is the amount of time needed for the pallet sensor to achieve to 90% of its initial baseline resistance following the removal of the analyte, whereas response time is typically defined as the amount of time needed for the sensor to reach up to 90% of its ultimate saturated value upon analyte introduction [45].

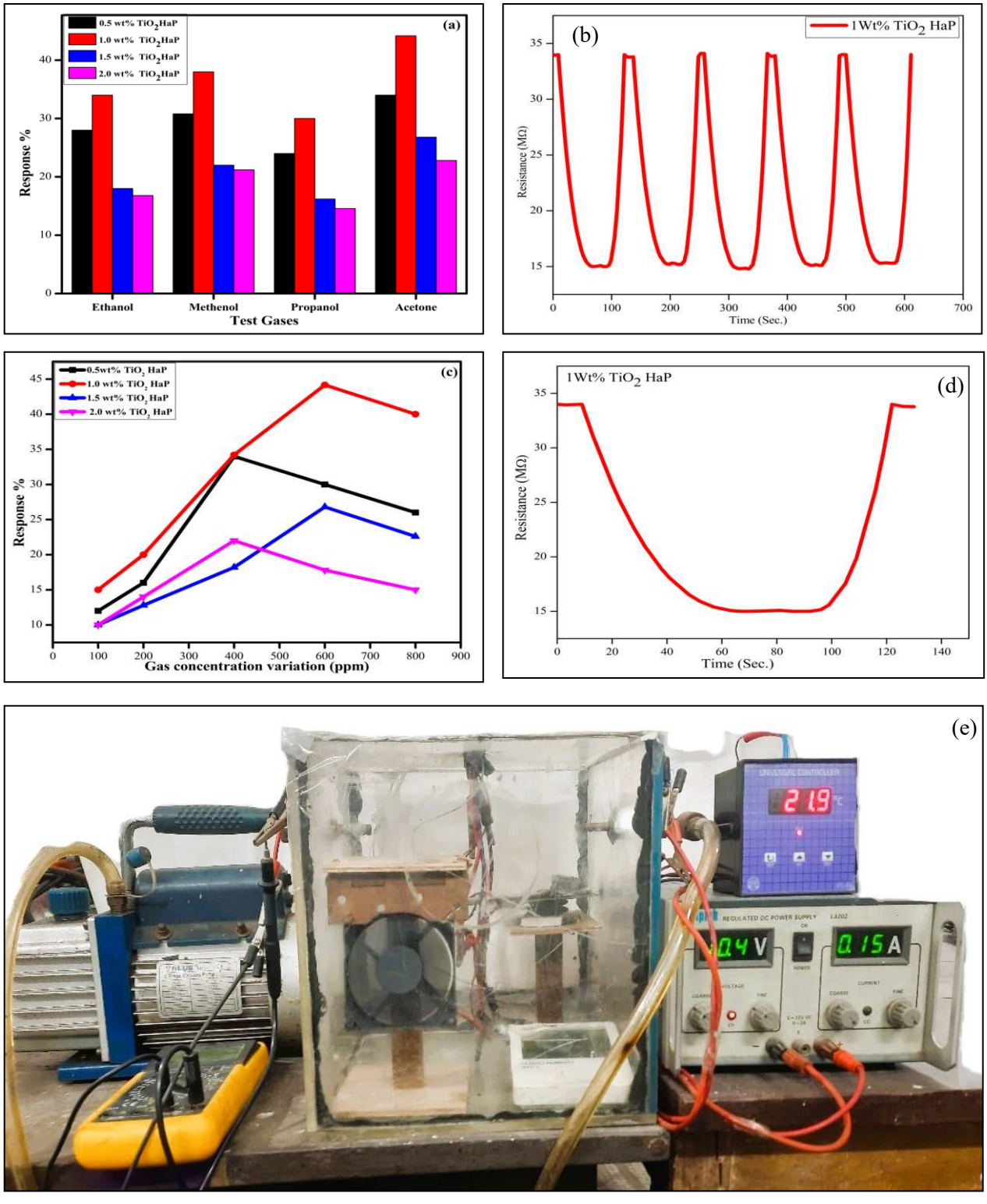


Fig.7 Investigation of TiO_2 dispersed HaP gas sensor (a) response of different wt% (0.5-2.0wt%) sample at 600ppm at different VOCs (b) repeatability graph between resistance and time at 600pmm acetone For 1 wt% composite (c) variation of gas sensor at different concentration of acetone (d) Response recovery curve 1wt% composite (e) Simple lab gas sensing setup

When tested at concentrations of 100–800 ppm, the sensor's response and recovery times show adsorption–desorption characteristics. Among the four VOCs, acetone exhibits the highest sensitivity in the 1wt% TiO_2-HaP composite at 600 ppm as seen in bar graph fig.7(a). It was observed that the baseline resistance (Ra) of a 1 weight percent TiO_2 distributed HaP pellet was roughly 34 MΩ in air. However, when exposed to acetone vapors at 600 ppm, the sample's resistance dropped to roughly 15 MΩ. The repeatability was verified since the sensor displayed the same resistance profiles during five consecutive adsorption–desorption cycles under the same environmental circumstances, as illustrated in Fig. 7 (c). The response increases monotonically as the percentage of acetone concentration increases from 100 ppm to 600 ppm, of the sensor as shown in Fig. 7(d), which shows response on analyte versus different concentration of VOCs of 1wt% TiO_2-HaP composite. This is because a larger electron release event and a greater displacement of adsorbed oxygen result from more vapor molecules vying for surface locations. Following that, as acetone increasingly occupies the active sites of the pallet under study, the response gradually decreases at higher concentrations from around 600 ppm to 800 ppm.

Further the hydroxyapetite's ($Ca_{10}(PO_4)_6(OH)_2$), have high porosity and strong ionic conductivity allow for the physisorption of VOC molecules [32]. Mobile hydroxyl OH^- ions and a variety of ionic groups, including Ca^{2+}, PO_4^{3-}, and P-OH species, are present in the hydroxyapatite [46]. When hydroxyl groups engage with HaP and contribute to the proton hopping pathway, oxide ions (O^{2-}) are formed on the sample's surface.

$$OH^- + OH^- \rightarrow O^{2-} + H_2O$$

and

$$OH^- + PO_4^{3-} \rightarrow O^{2-} + OH \rightarrow O^{2-} + PO_4^{3-} + H_2O + \text{Vacancy (OH ions)}$$

The presence of (O^{2-}) oxide ions on the sample's surface allows it to absorb electrons from acetone vapor, resulting in a notable change in conduction.

The free electrons in the TiO_2 conduction band interact with atmospheric oxygen molecules in ambient air, trapping them to create oxygen species and radicals at the TiO_2 surface. Because of the high Ra value found in air, this electron trapping reduces carriers near the surface conduction band, forming resistive depletion layer that increases the overall resistance of TiO_2 grains [47,48].The absorbed acetone molecules react with the O2-species when the

pallet base sensor is exposed to acetone vapor, devouring them and releasing the captured electrons back into the conduction band.

$$CH_3COCH_3 + 8O^- \leftrightarrow 3CO_2 + 3H_2O + 8e^-$$

The observed change in sensor resistance is caused by the return of electrons from the conduction band, which collapses the depletion layer and significantly lowers TiO_2 grain resistance. The amount of this impact increases with surface area, the concentration of acetone vapor in the chamber, and the number of accessible O^{2-}sites, which is dependent on TiO_2 loading. Ionic conduction and depletion layer mechanisms in TiO_2 dispersed HaP nanocomposite are driven by the combined chemical sensing effects of TiO_2 and HaP.

Thus the combined effect in pallete based composite sensor proven more reliable than the pure material. Among four wt% (0.5wt% - 2.0 wt%) TiO_2 - HaP nanocomposite, the 1.0 wt% composition exihibits superior response and recovery times, making it the most promising nanocomposite for acetone vapour sensing application.

5. Conclusion

The TiO_2-dispersed hydroxyapatite (HaP) nanocomposites were successfully synthesized and characterized using XRD, SEM, EDX, Raman and XPS, which confirmed the formation of the HaP phase with TiO_2 and indicated Ti–O–P interaction at the interface. The samples were tested as resistive sensors for ethanol, methanol, propanol and acetone. Among all compositions, the 1 wt% TiO_2/HaP sensor showed the best performance, with a response of 44.17% towards acetone at 600 ppm, along with response and recovery times of 62 s and 56 s. Its response to acetone was clearly higher than to the other three VOCs. This improvement is linked to the TiO_2/HaP interface, which provides more active sites and better oxygen adsorption. Thus, 1 wt% TiO_2/HaP is a low-cost and promising material for acetone sensing.

Acknowledgements The authors sincerely acknowledge the department of Physics (central instrumentation facility) of University of Lucknow for providing characterization support.

Author Contributions Ravi Kumar Pandey, synthesis and characterized the sample, investigate and draft the original manuscript, R. R. Awasthi and R. K. Shukla (Corresponding Author) review and editing the original manuscript.

Funding Authors received no funding for any funding agencies.

Data Availability All data are original and no data were generated or analysed during the current research study.

Declarations

Data Accessibility On request, data will be made available.

Competing Interests The authors declare no competing interests.

References:

1. Kusunoki, M., Sakoishi, Y., Makino, T., Tsunemine, T., Fujita, N., Okada, Y., & Hayami, T. (2019). Orientation control for a-axis or c-axis oriented crystal films of hydroxyapatite, and a possible growth mechanism derived from X-ray diffraction. *Applied Surface Science*, 484, 433-440. https://doi.org/ 10.1016/j.apsusc.2019.04.135

2. Narwade, V. N., Pottathara, Y. B., Begum, S., Lakhane, M. A., Tiyyagura, H. R., Khairnar, R. S., & Bogle, K. A. (2021). Nanostructured hydroxyapatite biomaterial as gas sensor. In *Nanoscale processing* (pp. 439-466). Elsevier. https://doi.org/10.1016/B978-0-12-820569-3.00016-5

3. Chatterjee, T., Das, A. K., Pradhan, S. K., & Meikap, A. K. (2020, November). Frequency dependent dielectric properties of silver doped hydroxyapatite nanoparticles. In *AIP Conference Proceedings* (Vol. 2265, No. 1, p. 030434). *AIP Publishing LLC*. https://doi.org/10.1063/5.0017392

4. Mahabole, M. P., Aiyer, R. C., Ramakrishna, C. V., Sreedhar, B., & Khairnar, R. S. (2005). Synthesis, characterization and gas sensing property of hydroxyapatite ceramic. *Bulletin of Materials Science*, *28*(6), 535-545. https://doi.org/10.1007/BF02706339

5. Nayak, A., & Bhushan, B. (2021). Hydroxyapatite as an advanced adsorbent for removal of heavy metal ions from water: Focus on its applications and limitations. *Materials Today: Proceedings*, *46*, 11029-11034.29 https://doi.org/ 10.1016/j.matpr.2021.02.149

6. Hernández-Cocoletzi, H., Salinas, R. A., Águila-Almanza, E., Rubio-Rosas, E., Chai, W. S., Chew, K. W., & Show, P. L. (2020). Natural hydroxyapatite from fishbone waste for the rapid adsorption of heavy metals of aqueous effluent. *Environmental Technology & Innovation*, *20*, 101109. https://doi.org/ 10.1016/j.eti.2020.101109

7. Brazdis, R. I., Fierascu, I., Avramescu, S. M., & Fierascu, R. C. (2021). Recent progress in the application of hydroxyapatite for the adsorption of heavy metals from water matrices. *Materials*, *14*(22), 6898. https://doi.org/ 10.3390/ma14226898

8. Pai, S., Kini, M. S., & Selvaraj, R. (2021). A review on adsorptive removal of dyes from wastewater by hydroxyapatite nanocomposites. *Environmental Science and Pollution Research*, *28*(10), 11835-11849. https://doi.org/10.1007/s11356-019-07319-9

9. Amor, G., Vázquez, A., González, L. T., Cordero-Segovia, S., Zorrilla-Siller, J., Kharissova, O. V., & Kharisov, B. I. (2026). Hydroxyapatite nanomaterials for environmental applications in wastewater treatment. In *Handbook of Nanomaterials and Nanocomposites for Energy and Environmental Applications* (pp. 1-27). Cham: Springer Nature Switzerland. https://doi.org/10.1007/978-3-030-11155-7_12-2

10. Balasooriya, I. L., Chen, J., Korale Gedara, S. M., Han, Y., & Wickramaratne, M. N. (2022). Applications of nano hydroxyapatite as adsorbents: a review. *Nanomaterials*, *12*(14), 2324. https://doi.org/10.3390/NANO12142324

11. Tripathi, A., Raj, R., Sathe, S. M., Surampalli, R. Y., & Ghangrekar, M. M. (2024). Reviewing the advancement of calcium hydroxyapatite-mediated treatment for the remediation of wastewater: applications, degradation kinetics and future perspective. *Clean Technologies and Environmental Policy*, *26*(11), 3697-3714. https://doi.org/10.1007/s10098-023-02576-2

12. Avola, T. (2025). Eco-friendly hydroxyapatite-based materials as metal adsorbents: optimization of surface properties for water and wastewater remediation.

13. Fatine, S., Laghzizil, A., & Nunzi, J. M. (2026). Functionalised hydroxyapatites for heavy metals removal from water: a review. *International Journal of Environmental Analytical Chemistry*, *106*(1), 73-90. https://doi.org/10.1080/03067319.2025.2510428

14. Bouyarmane, H., El Bekkali, C., Labrag, J., Es-Saidi, I., Bouhnik, O., Abdelmoumen, H., & Robert, D. (2021). Photocatalytic degradation of emerging antibiotic pollutants in waters by TiO2/Hydroxyapatite nanocomposite materials. *Surfaces and Interfaces*, *24*, 101155. https://doi.org/ 10.1016/j.surfin.2021.101155

15. Liu, Y., Liu, C. Y., Wei, J. H., Xiong, R., Pan, C. X., & Shi, J. (2010). Enhanced adsorption and visible-light-induced photocatalytic activity of hydroxyapatite modified Ag–TiO2 powders. *Applied Surface Science*, *256*(21), 6390-6394. https://doi.org/ 10.1016/j.apsusc.2010.04.022

16. Khairnar, R. S., Mene, R. U., Munde, S. G., & Mahabole, M. P. (2011, December). Nano-hydroxyapatite thick film gas sensors. In *AIP Conference Proceedings* 1415, 189-192. American Institute of Physics. https://doi.org/ 10.1063/1.3667253

17. Kanan, S., Obeideen, K., Moyet, M., Abed, H., Khan, D., Shabnam, A., & Mohamed, A. A. (2025). Recent advances on metal oxide based sensors for environmental gas pollutants detection. *Critical Reviews in Analytical Chemistry*, *55*(5), 911-944. https://doi.org/ 10.1080/10408347.2024.2325129

18. Baltrusaitis, J., Jayaweera, P. M., & Grassian, V. H. (2011). Sulfur dioxide adsorption on TiO_2 nanoparticles: influence of particle size, coadsorbates, sample pretreatment, and light on surface speciation and surface coverage. *The Journal of Physical Chemistry C*, *115*(2), 492-500. https://doi.org/10.1021/jp108759b

19. Pravarthana, D., Tyagi, A., Jagadale, T. C., Prellier, W., & Aswal, D. K. (2021). Highly sensitive and selective H2S gas sensor based on TiO2 thin films. *Applied Surface Science*, *549*,149281. https://doi.org/10.1016/j.apsusc.2021.149281

20. Li, W., Kan, K., He, L., Ma, L., Zhang, X., Si, J., ... & Shi, K. (2020). Biomorphic synthesis of 3D mesoporous SnO_2 with substantially increased gas-sensing performance at room temperature using a simple one-pot hydrothermal method. *Applied Surface Science*, *512*, 145657. https://doi.org/10.1016/j.apsusc.2020.145657

21. Begum, S., Narwade, V. N., Taha, S., Mahabole, M. P., Dadge, J. W., & Bogle, K. A. (2021, December). Hydroxyapatite-Graphene Oxide Nanocomposite with Enhanced Ammonia Sensing Property. In *Macromolecular Symposia*, 400, 2100165. https://doi.org/10.1002/masy.202100165

22. Dev, P. R., Anand, C. P., Michael, D. S., & Wilson, P. (2022). Hydroxyapatite coatings: a critical review on electrodeposition parametric variations influencing crystal facet orientation towards enhanced electrochemical sensing. *Materials Advances*, *3*(21), 7773-7809. https://doi.org/10.1039/D2MA00620K

23. Marques, J. R., Feitosa, R. P., De Lima, I. S., Oliveira, L. H., Silva-Filho, E. C., Franco, F., & Osajima, J. A. (2025). Enhanced Antibiotic Removal via Adsorption–Photocatalysis Using a ZnO–TiO2–Halloysite Nanocomposite. *Minerals*, 15(12), 1253. https://doi.org/10.3390/min15121253

24. Seekaew, Y., Wisitsoraat, A., Phokharatkul, D., & Wongchoosuk, C. (2019). Room temperature toluene gas sensor based on TiO_2 nanoparticles decorated 3D graphene-carbon nanotube nanostructures. *Sensors and Actuators B: Chemical*, *279*, 69-78. https://doi.org/10.1016/j.snb.2018.09.095

25. Sertel, B. C., Sonmez, N. A., Kaya, M. D., & Ozcelik, S. (2019). Development of MgO: TiO_2 thin films for gas sensor applications. *Ceramics International*, *45*(3), 2917-2921. https://doi.org/10.1016/j.ceramint.2018.11.079

26. Shooshtari, M., Vollebregt, S., Vaseghi, Y., Rajati, M., & Pahlavan, S. (2023). The sensitivity enhancement of TiO_2-based VOCs sensor decorated by gold at room temperature. *Nanotechnology*, *34*(25), 255501. https://doi.org/10.1088/1361-6528/acc6d7

27. Patil, V. L., Vanalakar, S. A., Shendage, S. S., Patil, S. P., Kamble, A. S., Tarwal, N. L., ... & Patil, P. S. (2019). Fabrication of nanogranular TiO_2 thin films by SILAR technique: Application for NO2 gas sensor. *Inorganic and Nano-Metal Chemistry*, *49*(7), 191-197. https://doi.org/ 10.1080/24701556.2019.1599948

28. KA, K. L., Nishanth, T., Puliyasseri, R., & Brinesh, R. (2026). Photochemical Dynamics of Surface Ozone (O_3), Carbon Monoxide (CO), and Nitrogen Oxides (NO_x): Implications for Air Pollution, Health and Climate. *International Journal of Atmospheric and Oceanic Sciences*, *10*(1), 13-24. https://doi.org/10.11648/j.ijaos.20261001.12

29. Insam, H., & Seewald, M. S. (2010). Volatile organic compounds (VOCs) in soils. *Biology and fertility of soils*, *46*(3), 199-213. https://doi.org/10.1007/s00374-010-0442-3

30. Ofudje, E. A., Adeogun, A. I., Idowu, M. A., & Kareem, S. O. (2019). Synthesis and characterization of Zn-Doped hydroxyapatite: scaffold application, antibacterial and bioactivity studies. *Heliyon,* 5(5). https://doi.org/10.1016/j.heliyon.2019.e01716

31. Kumar, S., Yadav, N., & Singh, P. (2024). Effect of graphene weight percentage on surface morphology and humidity-sensing performances of hydroxyapatite/graphene nanocomposite. *Journal of Materials Science: Materials in Electronics*, *35*(35), 2238.https://doi.org/ 10.1007/s10854-024-14019-9

32. Taha, S., Begum, S., Narwade, V. N., Halge, D. I., Dadge, J. W., Mahabole, M. P., & Bogle, K. A. (2020). Development of alcohol sensor using TiO_2-Hydroxyapatite nano-composites. *Materials Chemistry and Physics*, *240*, 122228. https://doi.org/ 10.1016/j.matchemphys.2019.122228

33. Pandey, P. K., Thareja, R. K., Singh, R. P., & Costello, J. T. (2018). Deposition of nanocomposite Cu–TiO2 using heterogeneous colliding plasmas. Applied Physics B, 124(3), 50. https://doi.org/10.1007/s00340-018-6919-8

34. Avinashi, S. K., Singh, P., Sharma, K., Hussain, A., Singh, D., & Gautam, C. (2022). Morphological, mechanical, and biological evolution of pure hydroxyapatite and its composites with titanium carbide for biomedical applications. *Ceramics International*, *48*(13), 18475-18489. https://doi.org/ 10.1016/j.ceramint.2022.03.117

35. Tsuda, H., & Arends, J. (1993). Detection and quantification of calcium fluoride using micro-Raman spectroscopy. *Caries Research*, *27*(4), 249-257. https://doi.org/ 10.1159/000261545

36. Rath, P. C., Besra, L., Singh, B. P., & Bhattacharjee, S. (2012). Titania/hydroxyapatite bi-layer coating on Ti metal by electrophoretic deposition: Characterization and corrosion studies. *Ceramics International*, *38*(4), 3209-3216. https://doi.org/ 10.1016/j.ceramint.2011.12.026

37. Zhao, H., Li, X., Wang, J., Qu, S., Weng, J., & Zhang, X. (2000). Characterization of peroxide ions in hydroxyapatite lattice. *Journal of biomedical materials research*, *52*(1), 157-163. https://doi.org/10.1002/1097-4636(200010)52:1<157::AID-JBM20>3.0.CO;2-UDigital Object Identifier (DOI)

38. Secundino-Sánchez, O., Diaz-Reyes, J., Sánchez-Ramírez, J. F., & Jiménez-Pérez, J. L. (2019). Structural and optical characterization of the crystalline phase transformation of electrospinning TiO2 nanofibres by high temperatures annealing. *Revista mexicana de fisica*, *65*(5), 459-467. https://doi.org/ 10.31349/revmexfis.65.459

39. Al-Taweel, S. S., & Saud, H. R. (2016). New route for synthesis of pure anatase TiO_2 nanoparticles via utrasound-assisted sol-gel method. *J. Chem. Pharm. Res*, *8*(2), 620-626.

40. Anwar, A., Kanwal, Q., Akbar, S., Munawar, A., Durrani, A., & Hassan Farooq, M. (2017). Synthesis and characterization of pure and nanosized hydroxyapatite bioceramics. *Nanotechnology Reviews*, *6*(2), 149-157. https://doi.org/10.1515/ntrev-2016-0020

41. Ciobanu, C. S., Predoi, D., Iconaru, S. L., Negrila, C. C., Leduc, D., Ghegoiu, L., ... & Predoi, M. V. (2025). New Nanobioceramics Based on Hydroxyapatite for Biomedical Applications: Stability and Properties. *Nanomaterials*, *15*(3), 224. https://doi.org/10.3390/nano15030224

42. Mahabole, M. P., Aiyer, R. C., Ramakrishna, C. V., Sreedhar, B., & Khairnar, R. S. (2005). Synthesis, characterization and gas sensing property of hydroxyapatite ceramic. *Bulletin of Materials Science*, *28*(6), 535-545. https://doi.org/10.1007/BF02706339

43. Zhu, L., Lu, Q., Lv, L., Wang, Y., Hu, Y., Deng, Z., ... & Teng, F. (2017). Ligand-free rutile and anatase TiO2 nanocrystals as electron extraction layers for high performance inverted polymer solar cells. *RSC advances*, *7*(33), 20084-20092. https://doi.org/10.1039/c7ra00134g

44. Didwal, P. N., Chikate, P. R., Bankar, P. K., More, M. A., & Devan, R. S. (2019). Intense field electron emission source designed from large area array of dense rutile TiO2 nanopillars. *Journal of Materials Science: Materials in Electronics*, *30*(3), 2935-2941. https://doi.org/10.1007/s10854-018-00570-9

45. Tripathi, S., Shukla, R. K., & Srivastava, A. (2025). Titanium-doped Graphene Oxide Nanocomposite Synthesis for Gas Sensing and VOCs Detection at Ambient Temperature. *Sensing and Imaging*, *26*(1), 55. https://doi.org/10.1007/s11220-025-00585-7

46. Mene, R. U., Mahabole, M. P., Sharma, R., & Khairnar, R. S. (2011). Enhancement in CO gas sensing properties of hydroxyapatite thick films: Effect of swift heavy ion irradiation. *Vacuum*, *86*(1), 66-71. https://doi.org/ 10.1016/j.vacuum.2011.04.015

47. Pandeeswari, R. K. K. R., Karn, R. K., & Jeyaprakash, B. G. (2014). Ethanol sensing behaviour of sol–gel dip-coated TiO_2 thin films. *Sensors and Actuators B: Chemical*, *194*, 470-477. https://doi.org/ 10.1016/j.snb.2013.12.122

48. Kwon, Y., Kim, H., Lee, S., Chin, I. J., Seong, T. Y., Lee, W. I., & Lee, C. (2012). Enhanced ethanol sensing properties of TiO_2 nanotube sensors. *Sensors and Actuators B: Chemical*, *173*, 441-446. https://doi.org/ 10.1016/j.snb.2012.07.062